Fraction of delocalized eigenstates in the long-range Aubry-André-Harper model

Nilanjan Roy ⬤ and Auditya Sharma

Department of Physics, Indian Institute of Science Education and Research, Bhopal, Madhya Pradesh 462066, India

We uncover a systematic structure in the single-particle phase diagram of the quasiperiodic Aubry-André-Harper (AAH) model with power-law hoppings ($\sim \frac{1}{r^\sigma}$) when the quasiperiodicity parameter is chosen to be a member of the metallic mean family of irrational Diophantine numbers. In addition to the fully delocalized and localized phases, we find a coexistence of multifractal (localized) states with the delocalized states for $\sigma < 1$ ($\sigma > 1$). The fraction of delocalized eigenstates in these phases can be obtained from a general sequence, which is a manifestation of a mathematical property of the metallic mean family. The entanglement entropy of the noninteracting many-body ground states respects the area law if the Fermi level belongs in the localized regime while logarithmically violating it if the Fermi level belongs in the delocalized or multifractal regimes. The prefactor of the logarithmically violating term is significantly larger in the delocalized phase in comparison to that in the multifractal phase. Entanglement entropy shows the area law even in the delocalized regime for special filling fractions, which are related to the metallic means.

I. INTRODUCTION

Quasiperiodic systems or quasicrystals lie at the junction of periodic and random systems and exhibit nontrivial intermediate localization properties [1–4]. Unlike the one-dimensional Anderson model [5], where even an infinitesimal random potential leads to localization, a nonzero finite quasiperiodic potential is essential for the Aubry-André-Harper (AAH) model to show a delocalization-localization transition in one dimension [6,7]. Remarkably, even the presence of a mobility edge (which in the traditional Anderson model can be seen only in three dimensions) has been reported in variants of the AAH model [8,9] even in one dimension. The AAH potential has been realized in experiments of ultracold atoms studying single-particle localization [10–12] and many-body localization [13], which has led to a fresh wave of interest in quasiperiodic systems at zero [14–20] and finite temperatures [21–23] in recent times. On the other hand, the study of Hamiltonians with power-law hoppings or interactions ($\propto \frac{1}{r^\sigma}$) has seen a resurgence of interest after such Hamiltonians were realized in experiments of ultracold systems [24–35]. When the hopping strength is sufficiently long ranged, instead of the exponentially localized eigenstates seen in short-range models, one may obtain algebraically localized eigenstates [36–39]. Despite the rich literature on both quasiperiodic and long-range systems, the interplay of both these aspects has only begun to be studied [40–43].

The effect of power-law hoppings which breaks the self-duality of the quasiperiodic AAH potential has been studied recently [40]. This study has shown the appearance of multifractal (localized) eigenstates which coexist with delocalized eigenstates for $\sigma < 1$ ($\sigma > 1$) [40]. The irrationality of the quasiperiodicity parameter (α) which renders the Hamiltonian quasiperiodic is key to the striking physics of this system.

In the present paper, we show, with the aid of a transparent prescription, the relationship between the fraction of delocalized eigenstates in the different phases of the system and the parameter α. While most studies of the AAH model choose this irrational number to be the golden mean ($\sqrt{5} - 1)/2$, we obtain a general result for a broader class of irrational Diophantine numbers, referred to as the metallic mean family, of which the golden mean is just one element.

In this paper, we chart out the phase diagram of a single particle in the presence of the AAH potential and power-law hoppings when α is set to be a member of the metallic mean family, with special attention given to the golden mean, silver mean, and bronze mean. In addition to the delocalized and localized phases, we obtain mixed phases where the multifractal (localized) states can coexist with delocalized states for $\sigma < 1$ ($\sigma > 1$). One of the key findings of our paper is that the fraction of delocalized eigenstates in these phases can be obtained from a general sequence, which is related to a mathematical property of the metallic means (see schematic in Fig. 1). Moreover, we study the subsystem size scaling of entanglement entropy [44,45] of the noninteracting fermionic many-body ground states to characterize different phases in the model. The delocalized and multifractal Fermi level show logarithmic violation of the area law of entanglement entropy with different prefactors in the logarithm term. The prefactor is found to vary in different phases. In the delocalized regime, entanglement entropy is surprisingly found to follow the area law for certain special filling fractions which are related to the metallic means. We show that such strange behavior at the special filling fractions [46] may be understood from the single particle spectrum.

The paper is organized as follows. In Sec. II, we describe the model and metallic means. In Sec. III, we derive the single
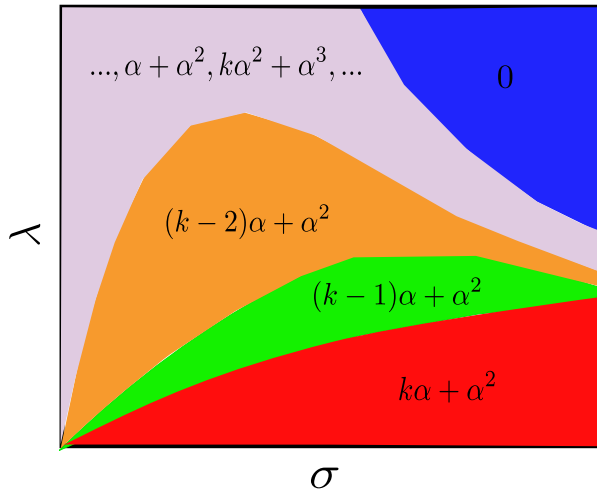
FIG. 1. Schematic of the phases of a single particle in the LRH model for the quasiperiodicity parameter α, shown in different colors. The colored phases are also labeled by the fraction of delocalized eigenstates (η) as shown in the figure. Here $k = 1, 2, 3$ when α is golden mean, silver mean, and bronze mean, respectively. The strength of the quasiperiodic potential and power-law hopping parameter are denoted as λ and σ, respectively.

particle phase diagram for metallic means by analyzing fractal dimension and inverse participation ratio (IPR) of the eigenstates. In Sec. IV, we show a general sequence to obtain the fraction of delocalized states in different phases. In Sec. V, we analyze the scaling of the ground-state entanglement entropy of noninteracting fermions to characterize the phases. Then we conclude in Sec. VI.

II. THE MODEL

The model of interest is the one-dimensional long-range AAH (LRH) model given by the Hamiltonian

$$H = -\sum_{i<j}^{N} \left(\frac{J}{r_{ij}^{\sigma}} \hat{c}_i^{\dagger} \hat{c}_j + \text{H.c.} \right) + \lambda \sum_{i=1}^{N} \cos(2\pi\alpha i + \theta_p)\hat{n}_i, \quad (1)$$

where $\hat{c}_i^{\dagger}$ ($\hat{c}_i$) represents the single particle creation (destruction) operator at site i and corresponding number operator $\hat{n}_i = \hat{c}_i^{\dagger}\hat{c}_i$. We consider a lattice of total number of sites N, where r_{ij} is the geometric distance between the sites i and j in a ring. Here λ is the strength of the quasiperiodic potential with the parameter α chosen to be a Diophantine irrational number [47], e.g., $(\sqrt{5}-1)/2$. θ_p is an arbitrary global phase. The strength of the long range hopping is controlled by J and the long range parameter in the hopping σ. We will assume $J = 1$ for all the numerics. In the $\sigma \to \infty$ limit this model becomes the celebrated AAH model [6,7]. As a consequence of self-duality [6,7], all the eigenstates are delocalized for $\lambda < 2J$ and localized for $\lambda > 2J$ [47]. For a finite σ, self-duality is broken.

A. Metallic mean family

Any irrational number can be written as a continued fraction [48] which allows for a successive rational approximation

of it in the form of a/b where a, b are co-prime numbers. For Diophantine numbers, there always exists a lower bound to how closely such irrational numbers may be represented by rational approximations, such that $|\alpha - \frac{a}{b}| > \epsilon/b^{2+\zeta}$ with $\epsilon > 0$ and $\zeta \geqslant 0$ [49,50]. The above property is a sign of the strength of the irrationality of Diophantine numbers.

It is useful to consider a generalized k-Fibonacci sequence [51], given by

$$F_u = kF_{u-1} + F_{u-2}, \quad (2)$$

with $F_0 = 0$, $F_1 = 1$. The limit $\alpha = \lim_{u\to\infty} F_{u-1}/F_u$ with $k = 1, 2, 3 \dots$ yields the metallic mean family, the first three members of which are the well-known golden mean ($\alpha_g = (\sqrt{5}-1)/2$), the silver mean ($\alpha_s = \sqrt{2}-1$), and bronze mean $\alpha_b = (\sqrt{13}-3)/2$, respectively. A slowly converging sequence of rational approximations of these Diophantine numbers is given by F_{u-1}/F_u for two successive members in the sequence for a fixed integer k. Each member α of the metallic mean family satisfies the following relation:

$$(\alpha)^z = k(\alpha)^{z+1} + (\alpha)^{z+2}, \quad (3)$$

where $k = 1, 2, 3 \dots$ for $\alpha = \alpha_g, \alpha_s, \alpha_b, \dots$, respectively, and z is a non-negative integer. Putting $z = 0$ in Eq. (3) also yields an important case, namely, $k\alpha + \alpha^2 = 1$.

III. SINGLE PARTICLE PROPERTIES

Now we consider a single particle in the LRH model with different parameters α_g, α_s, and α_b which are members of the metallic mean family. To determine the phases, we calculate the fractal dimension and IPR of the eigenstates for $\theta_p = 0$.

A. Fractal dimension

We employ the box counting procedure to determine the fractal dimension [52–55]. Dividing the system of N sites into $N_l = N/l$ boxes of l sites each, the fractal dimension is defined as

$$D_f = \lim_{\delta\to 0} \frac{1}{f-1} \frac{\ln \sum_{m=1}^{N_l} (\mathcal{I}_m)^f}{\ln \delta}, \quad (4)$$

where $\mathcal{I}_m = \sum_{i\in m} |\psi_n(i)|^2$ computed inside the mth box for the nth eigenstate $|\psi_n\rangle$ and $\delta = 1/N_l$. In the perfectly delocalized (localized) phase D_f is unity (zero), whereas for a multifractal state D_f shows a nontrivial dependence on f and $0 < D_f < 1$.

Figures 2(a)–2(c) show D_2 as a function of λ for all single-particle eigenstates when the quasiperiodicity parameter is fixed at α_g for $\sigma = 0.5, 1.5$, and 3.0, respectively. As can be seen from Fig. 2(a) for $\sigma = 0.5$, the fraction of delocalized eigenstates decreases and fractal states ($0 < D_2 < 1$) appear in blocks as λ increases. It turns out that these states are actually multifractal, which we discuss later (see Fig. 3). Hence there exists a delocalized-to-multifractal (DM) edge in the eigenstate spectrum. The DM edge goes down in steps as the fraction of delocalized eigenstates decreases with λ. However, the position of the DM edge remains unchanged within each step as the fraction of delocalized eigenstates (denoted as η hereafter) stays constant in that region. It is found that in the decreasing steplike regions defined by constant DM edges,
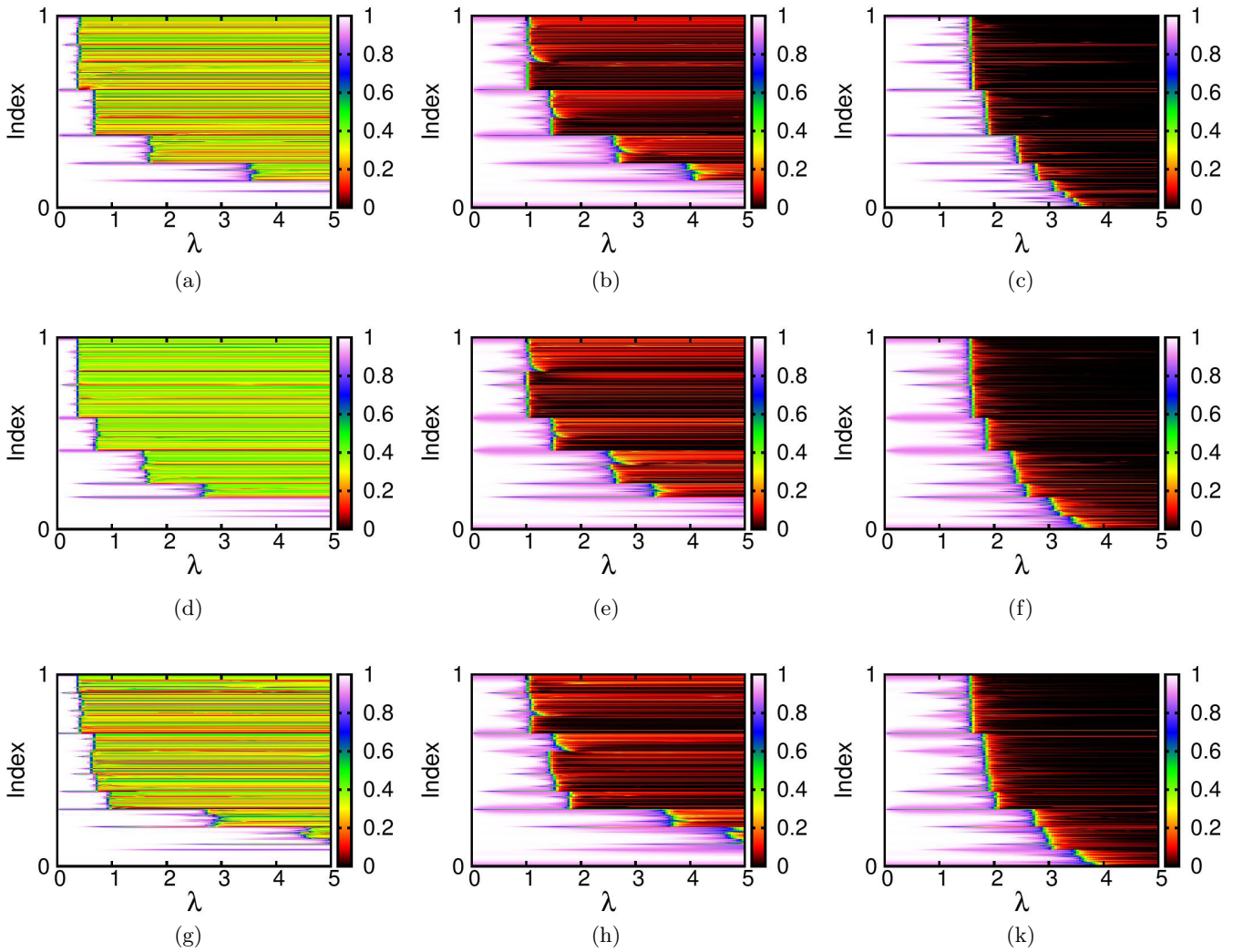
FIG. 2. (a)–(c) Fractal dimension D_2 (in color) as a function of λ and increasing fractional eigenstate index n/N starting from the ground state for α_g and $\sigma = 0.5, 1.5$, and 3.0, respectively. (d)–(f) Same plots for α_s. (g)–(k) Same plots for α_b. For all the plots, $N = 1000$ and $\delta = 0.02$.

$\eta = \alpha_g, \alpha_g^2, \alpha_g^3, \ldots$. We denote the steplike regions as P_q ($q = 1, 2, 3, \ldots$) phases with $\eta = \alpha_g, \alpha_g^2, \alpha_g^3, \ldots$, respectively.
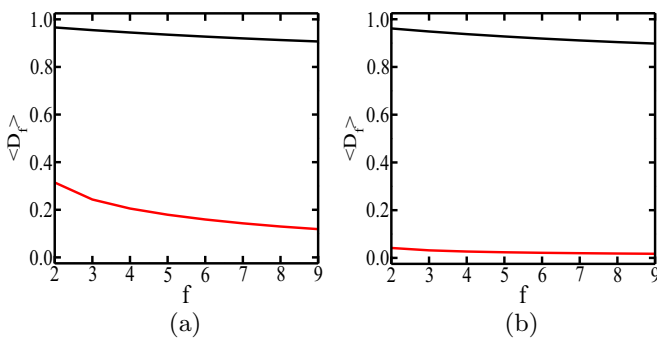

FIG. 3. (a) Averaged $\langle D_f \rangle$ as a function of f for $\lambda = 1.0$ and $\sigma = 0.5$ for which the system is in the P_2 phase with a DM edge. (b) Similar plots for $\lambda = 2.0$ and $\sigma = 1.5$ for which the system is in the P_2 phase with a DL edge. $\langle D_f \rangle$ is calculated by averaging over α_g^2 fraction of delocalized and $(1 - \alpha_g^2)$ fraction of multifractal/localized eigenstates. For all plots, system size $N = 987$ and $\delta = 1/N_l = 0.02$.

Figures 2(b) and 2(c) for $\sigma = 1.5$ and 3.0, respectively, show the appearance of blocks of localized states ($D_2 \approx 0$) with increasing λ. This implies that there exists a delocalized-to-localized (DL) edge, also well known as the mobility edge. Similar to DM edges, these fixed DL edges containing phases are also denoted as P_q ($q = 1, 2, 3, \ldots$) for $\eta = \alpha_g, \alpha_g^2, \alpha_g^3, \ldots$, respectively. D_2 of all the eigenstates for α_s and increasing λ is shown in Figs. 2(d)–2(f) for $\sigma = 0.5, 1.5, 3.0$, respectively. For α_s, one obtains $P_1, P_2, P_3, \ldots$ phases with $\eta = \alpha_s + \alpha_s^2, \alpha_s, \alpha_s^2 + \alpha_s^3, \ldots$ and DM edges (for $\sigma = 0.5$) and DL edges (for $\sigma = 1.5, 3.0$). Similarly, from Figs. 2(g)–2(k), for α_b and $\sigma = 0.5, 1.5, 3.0$, respectively, one obtains $P_1, P_2, P_3, \ldots$ phases with $\eta = 2\alpha_b + \alpha_b^2, \alpha_b + \alpha_b^2, \alpha_b, \ldots$ and DM edges (for $\sigma = 0.5$) and DL edges (for $\sigma = 1.5, 3.0$).

As evidence for multifractality, we plot $\langle D_f \rangle$ as a function of f for the P_2 phase (with α_g^2 fraction of delocalized states) for $\sigma = 0.5$ [in Fig. 3(a)] and $\sigma = 1.5$ [in Fig. 3(b)] in the LRH model with the golden mean α_g. Here $\langle D_f \rangle$ denotes D_f averaged over α_g^2 fraction of delocalized and $(1 - \alpha_g^2)$ fraction of nondelocalized eigenstates. We chose a Fibonacci system
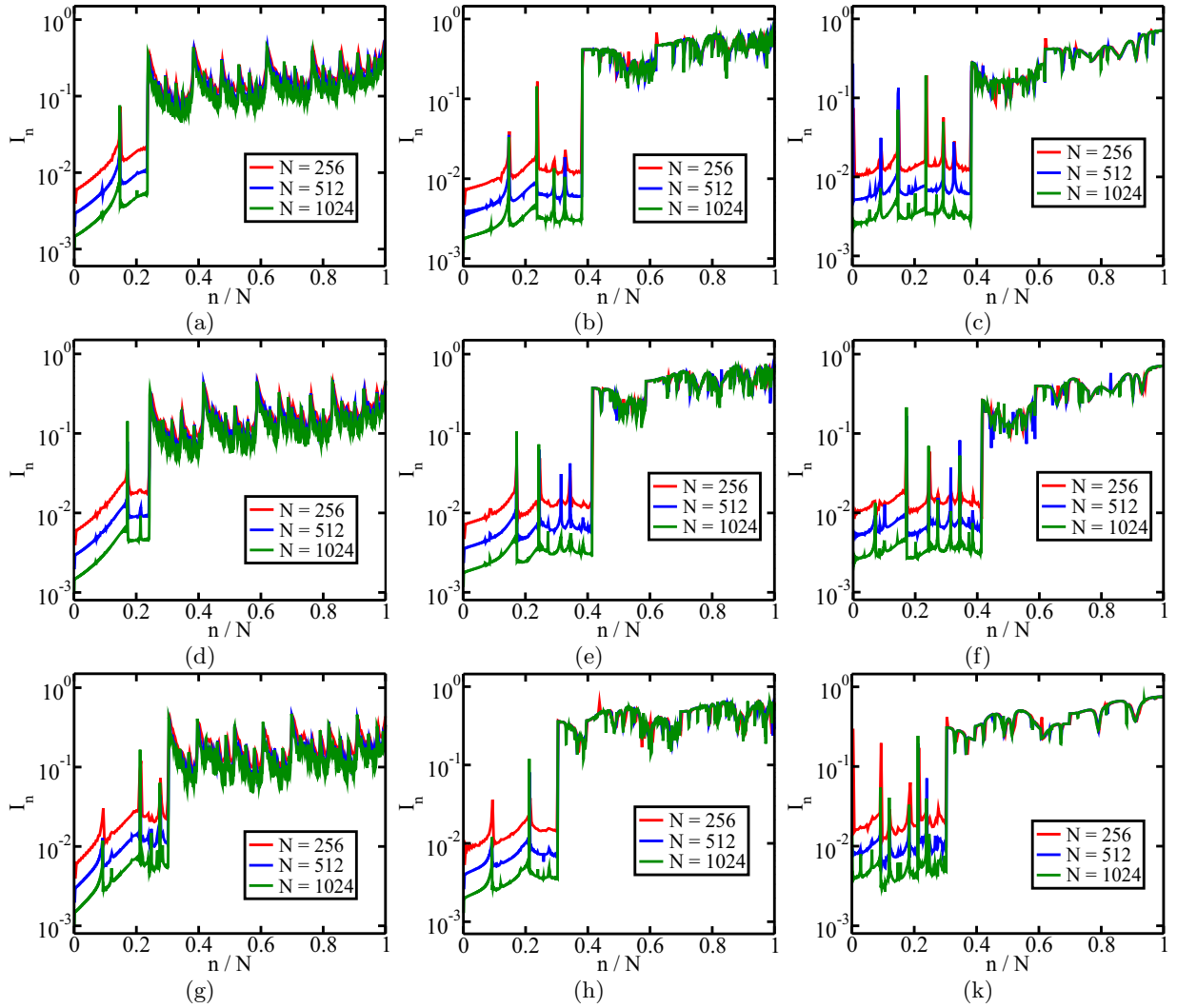
FIG. 4. (a)–(c) The inverse participation ratio I_n of the single-particle eigenstates for $\alpha_g = (\sqrt{5}-1)/2$ with increasing system sizes $N = 256, 512, 1024$ for $\sigma = 0.5, 1.5$ and 3.0, respectively. (d)–(f) Similar plots for $\alpha_s = (\sqrt{2}-1)$ with increasing N for $\sigma = 0.5, 1.5$, and 3.0, respectively. (h)–(k) Similar plots for $\alpha_b = (\sqrt{13}-3)/2$ with increasing N for $\sigma = 0.5, 1.5$, and 3.0, respectively. For all plots, λ is kept fixed at $\lambda = 2.2$. n/N is the fractional eigenstate index.

size $N = 987$ to reduce the fluctuations due to high-IPR eigenstates in the delocalized phase (see Appendix). In Figs. 3(a) and 3(b), $\langle D_f \rangle$ averaged over α_g^2 fraction of eigenstates shows a similar small variation with f with $\langle D_f \rangle$ being close to 1, which implies these states are delocalized. $\langle D_f \rangle$ averaged over $(1 - \alpha_g^2)$ fraction of eigenstates is a fraction and shows a nontrivial dependence on f for $\sigma = 0.5$ whereas $\langle D_f \rangle$ is close to 0 and shows almost no dependence on f for $\sigma = 1.5$. This indicates that these states are multifractal for $\sigma = 0.5$ and localized for $\sigma = 1.5$. Similar states can be found in the other P_q phases corresponding to α_s and α_b.

B. Inverse participation ratio

The IPR is a key quantity for studying delocalization-localization transitions. It is defined as

$$I_n = \sum_{i=1}^{N} |\psi_n(i)|^4, \qquad (5)$$

where the nth normalized single particle eigenstate $|\psi_n\rangle = \sum_{i=1}^{N} \psi_n(i) |i\rangle$ is written in terms of the Wannier basis $|i\rangle$, representing the state of a single particle localized at the site i of the lattice. For a delocalized eigenstate $I_n \propto N^{-1}$ whereas for a localized eigenstate $I_n \propto N^0$. For a critical state I_n shows intermediate behavior. Here we calculate IPR of the eigenstates for the LRH model with finite σ. To get a hint about the phases in the model, here we choose a fixed $\lambda = 2.2$ (which corresponds to the localized phase in the $\sigma \to \infty$ limit) and different values of $\sigma = 0.5, 1.5, 3.0$ for quasiperiodicity parameters α_g, α_s and α_b. The IPR of all the single particle eigenstates for α_g are shown in Figs. 4(a)–4(c) for $\sigma = 0.5, 1.5$, and 3.0, respectively. Figure 4(a) shows that the eigenstates are delocalized ($I_n \propto N^{-1}$) as long as the fractional index $n/N < \alpha_g^3$. The IPR of the remaining eigenstates for $n/N > \alpha_g^3$ shows an intermediate dependence on N, i.e., $N^{-1} < I_n < N^0$. It turns out that these eigenstates are multifractal [40] [see Fig. 3(a)]. Hence a DM edge exists at $n/N = \alpha_g^3$ for $\sigma = 0.5$ and $\lambda = 2.2$. As shown in
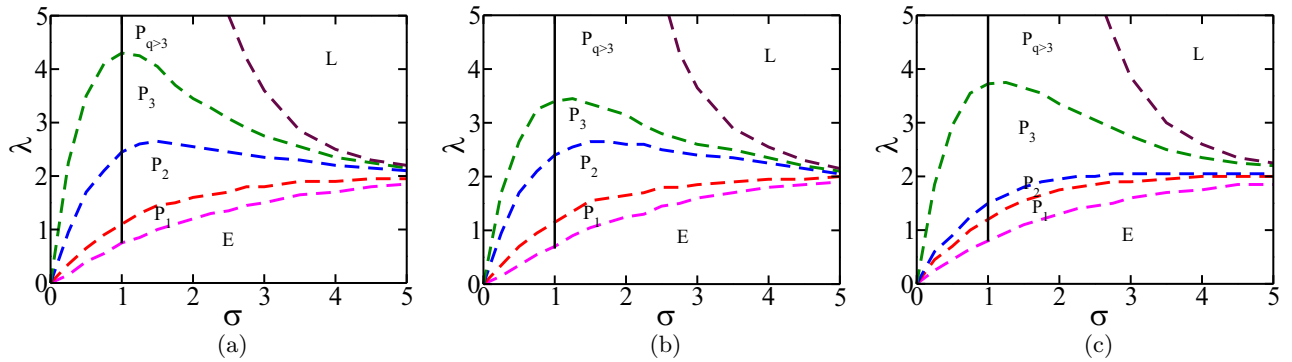
FIG. 5. Phase diagram: In addition to extended (E) and localized (L) phases with $\eta = 1, 0$, respectively, presence of the mixed phases with fractional η: $P_1, P_2, P_3, \ldots$ phases with (a) $\eta = \alpha_g, \alpha_g^2, \alpha_g^3, \ldots$; (b) $\eta = \alpha_s + \alpha_s^2, \alpha_s, \alpha_s^2 + \alpha_s^3, \ldots$; (c) $\eta = 2\alpha_b^2 + \alpha_b, \alpha_b^2 + \alpha_b, \alpha_b, \ldots$ are indicated. The vertical line separates out the DM edge for $\sigma < 1$ from the DL edge for $\sigma > 1$. (a)–(c) are for $\alpha_g, \alpha_s, \alpha_b$, respectively.

Figs. 4(b) and 4(c), the eigenstates are delocalized for $n/N < \alpha_g^2$ whereas the eigenstates are localized ($I_n \propto N^0$) for $n/N > \alpha_g^2$ for the same λ and $\sigma = 1.5$ and 3.0, respectively. This implies that there exists a DL (mobility) edge for $\lambda = 2.2$ and $\sigma = 1.5, 3.0$. Also we notice that the fraction of the delocalized eigenstates can change with σ for a fixed λ. However, the occasional presence of the high-IPR states as discussed for the AAH model (see Appendix), especially in the delocalized regime are also visible for the LRH model, since values of N are chosen to be non-Fibonacci numbers in all the plots of Fig. 4.

We also show the results obtained from the LRH model for the silver and bronze means. Plots obtained using α_s and $\lambda = 2.2$ are shown in Figs. 4(d)–4(f) for $\sigma = 0.5, 1.5$, and 3.0, respectively. These figures indicate that there is a DM edge at $n/N \approx \alpha_s^2 + \alpha_s^3$ for $\sigma = 0.5$ whereas there is a DL edge at $n/N \approx \alpha_s$ for $\sigma = 1.5$ and 3.0. Figures 4(g)–4(k) are obtained using fixed $\alpha_b, \lambda = 2.2$ for $\sigma = 0.5, 1.5$, and 3.0, respectively. It can be seen from Figs. 4(g)–4(k) that there is a DM edge at $n/N \approx \alpha_b$ for $\sigma = 0.5$ whereas a DL edge exists at $n/N \approx \alpha_b$ for $\sigma = 1.5$ and 3.0. We see that in every plot of Fig. 4 the fraction of delocalized eigenstates can always be expressed as a function of the parameter α. However, the IPR fluctuations due to the presence of the high-IPR states in the delocalized regime continue to persist in these cases also, although they tend to vanish if N is a Fibonacci number as can be seen in the AAH model (see Appendix). It is noticeable that the IPR fluctuations increase in the delocalized regime with σ.

C. Phase diagram

After an extensive analysis, we find that in a particular P_q phase, the same blocks of multifractal states become localized as one crosses $\sigma = 1$ whereas the corresponding η remains the same. We chart out the single-particle phase diagram for the parameter α_g in Fig. 5(a), which is also obtained in Ref. [40] for a Fibonacci N. Figures 5(a)–5(c) contain special states with high-IPR eigenstates, similar to the AAH model (see Appendix), even in the delocalized regimes. It is to be noted that as σ increases the extent of the mixed phases shrinks as the LRH model approaches the AAH limit. The phase diagrams for α_s and α_b are shown in Figs. 5(b) and 5(c), respectively. The P_q phases (corresponding to α_s and α_b) in these cases as

well, like with α_g, contain DM edges for $\sigma < 1$ and DL edges for $\sigma > 1$. The changes in P_q phases at $\sigma = 1$ are denoted by the vertical lines in all phase diagrams.

IV. FRACTION OF DELOCALIZED STATES

After a careful observation of the phase diagrams, one may propose a sequence which dictates the values of η in P_q phases corresponding to different quasiperiodicity parameters α, which belong to the metallic mean family described in Eq. (2). For any $\sigma > 0$ without disorder ($\lambda = 0$), $\eta = k\alpha + \alpha^2 = 1$, where $k = 1, 2, 3$ correspond to $\alpha_g, \alpha_s, \alpha_b$, respectively, and $z = 0$ in Eq. (3). As the quasiperiodic disorder is turned on ($\lambda \neq 0$), η starts decreasing in a sequence according to Eq. (3) for the metallic mean family, which is depicted in Fig. 6. Equation (3) implies that one can always express $(\alpha)^z$ as a sum of two bits $k(\alpha)^{z+1}$ and $(\alpha)^{z+2}$. In the LRH model, the bigger bit loses weight at every step becoming $(k-1)\alpha^{z+1}, (k-2)\alpha^{z+1}, \ldots$ until it reaches α^{z+1}, where it disintegrates again according to the rule defined in Eq. (3) and the new bigger bit starts losing weight at each step. This is a continuous process as depicted by the sequence in Fig. 6. For a specific choice of α, one obtains a P_q phase at each step of the sequence. The top of the sequence corresponds to the fully delocalized ($\eta = 1$) phase. One obtains $P_1, P_2, \ldots$ phases as one goes down following the sequence. The P_q phases possess DM (DL) edges if $\sigma < 1$ ($\sigma > 1$).

We show a schematic of the phase diagram in Fig. 1, where the colored regions are labeled by η in different phases. Choosing $k = 2$ in the sequence depicted in Fig. 6 leads to the phases labeled by η in Fig. 1. These phases are as follows → red: $\eta = 2\alpha + \alpha^2 = 1$ (delocalized); green: $\eta = \alpha + \alpha^2$ (P_1); orange: $\eta = 2\alpha^2 + \alpha^3$ (P_2); purple: $\eta = \alpha^2 + \alpha^3, 2\alpha^3 + \alpha^4, \ldots$ ($P_3, P_4 \ldots$, respectively) collectively, which appear as one proceeds further according to the sequence. For large values of σ and λ, the localized phase appears when $\eta = 0$, shown in blue.

V. ENTANGLEMENT ENTROPY

Here we consider noninteracting spinless fermions in the LRH model to calculate the entanglement entropy of the fermionic ground states in different phases obtained in the

$$ka + a^2 = 1$$

$$\downarrow$$

$$(k-1)a + a^2$$

$$\downarrow$$

$$(k-2)a + a^2$$

$$\downarrow$$

$$a + a^2 \quad \overset{a = ka^2 + a^3}{\downarrow}$$

$$ka^2 + a^3$$

$$\downarrow$$

$$(k-1)a^2 + a^3$$

$$\downarrow$$

$$(k-2)a^2 + a^3$$

$$\downarrow$$

$$a^2 + a^3 \quad \overset{a^2 = ka^3 + a^4}{\downarrow}$$

$$ka^3 + a^4$$

$$\downarrow$$

$$\downarrow$$

FIG. 6. Depicts how the fraction of delocalized eigenstates (η) decreases in a manner that uses the rule defined in Eq. (3). One can express the fraction of the delocalized states as a sum of two bits ka^{z+1} and a^{z+2}, out of which the bigger bit loses weight at every step until it reaches a^{z+1}, where it disintegrates according to the rule defined in Eq. (3) and then the bigger bit loses weight at each step. For a specific value of a, at every step of the sequence one obtains a P_q phase.

previous section. The entanglement entropy in the ground state of such free fermionic systems is given by [56–58]

$$S_A = -\sum_{m=1}^{L} [\zeta_m \ln \zeta_m + (1 - \zeta_m) \ln(1 - \zeta_m)], \quad (6)$$

where ζ_m's are the eigenvalues of the correlation matrix C^A, where $C_{ij}^A = \langle c_i^\dagger c_j \rangle$ with $i, j \in$ subsystem A of L sites. For free fermions in d dimensions, typically, $S_A \propto L^{d-1} \ln L$ in metallic phases [59], while it goes as $S_A \propto L^{d-1}$ in adherence to the area-law in the localized phases in the presence of disorder.

To produce smoother plots, we employ an average of S_A over the 100 realizations of θ_p uniformly choosing from $[0, 2\pi]$ in all the plots here. We stick to filling fraction $\nu = 0.5$ of fermions unless otherwise mentioned and $\alpha_g = (\sqrt{5} - 1)/2$. The S_A vs L plots are shown in Figs. 7(a) and 7(b) at half filling with increasing values of λ for $\sigma = 0.5$ and 1.5, respectively. A generic scaling form $S_A = K \ln L + K_0$ is assumed for this purpose. In Fig. 7(a), concentrating on $\sigma = 0.5$, when $\lambda = 0.1$ and 0.5 (delocalized and P_1 phases), the Fermi level is delocalized and hence $S_A \propto \ln L$ with $K \approx 0.32$ and 0.25, respectively. In the same figure, when $\lambda = 1.0$ and 2.0 (P_2 and P_3 phases) the Fermi level is multifractal,
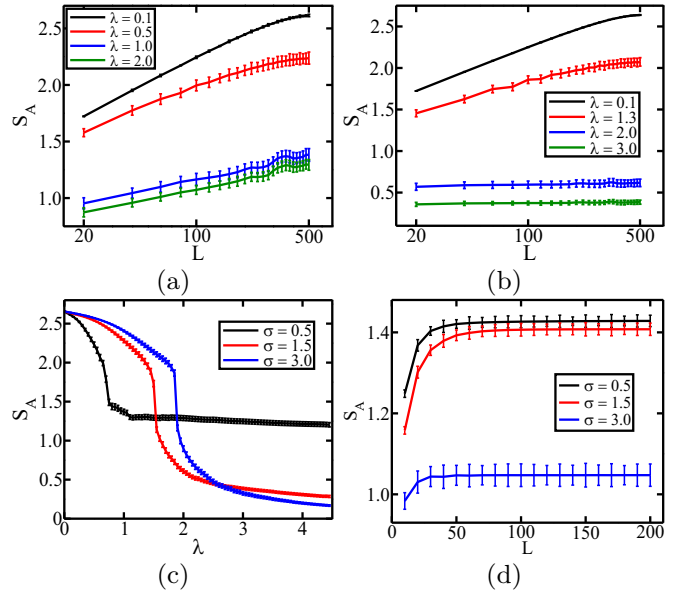

FIG. 7. (a), (b) The subsystem size L dependence of entanglement entropy S_A with increasing values of λ for fermions at half filling and for $\sigma = 0.5$ and 1.5. (c) S_A as function of λ for $\sigma = 0.5, 1.5,$ and 3.0, respectively, for fermions at half filling with $L = N/2$. For all plots in (a)–(c), $N = 1024$. (d) Entanglement entropy S_A as a function of subsystem size L for increasing σ and fixed $\lambda = 2.2$. For all plots, $N = 512$ for α_g and special filling $\nu = \alpha_g^4$.

$S_A \propto \ln L$ but the magnitude of S_A is drastically lower with $K \approx 0.13$. The logarithmic scaling behavior indicates that the multifractal states are essentialling extended states but with nonergodicity. The nonergodicity is reflected in the low magnitude of the prefactor in comparison with the ergodic extended/delocalized states. In Fig. 7(b), for $\sigma = 1.5$, when $\lambda = 0.1$ and 1.3 (delocalized and P_1 phases), the Fermi level is delocalized and $S_A \propto \ln L$ with $K \approx 0.33$ and 0.24, respectively. However, when $\lambda = 2.0$ and 3.0 (P_2 and P_3 phases) the Fermi level is localized, the magnitude of S_A is much lower, and it abides by the area law ($K \approx 0$). Transitions of Fermi level at half filling are shown in Fig. 7(c) for $\sigma = 0.5, 1.5,$ and 3.0, respectively. For $\sigma = 0.5$, the Fermi level undergoes a DM transition at $\lambda = 0.75$. For $\sigma = 1.5$ and 3.0, the Fermi level undergoes DL transitions at $\lambda = 1.5$ and $\lambda = 1.85$, respectively, as also evident from Figs. 2(a)–2(c).

We have also checked that the qualitative behavior of S_A versus L plots in the half-filled free fermionic ground state barely changes in the phase diagram for α_s and α_b. However, similar to the AAH model [46] (see Appendix), the LRH model too shows area-law behavior for special fillings ν even in the delocalized regime. An example of this is shown in Fig. 7(d) for $\lambda = 2.2$ and $\sigma = 0.5, 1.5, 3.0,$ and special filling $\nu = \alpha_g^4$. In all these plots, S_A abides by the area law. However, the magnitude of S_A is significantly smaller for $\sigma = 3.0$. We point out that while the single particle results depend on whether the system size is a Fibonacci number, the many-particle measures do not show such a dependence on the system size (see Appendix for details).

Next we further analyze the prefactor K of the log term from the subsystem size dependence of S_A for α_g. In Fig. 8(a), we show K as a function of λ for increasing values of σ for the
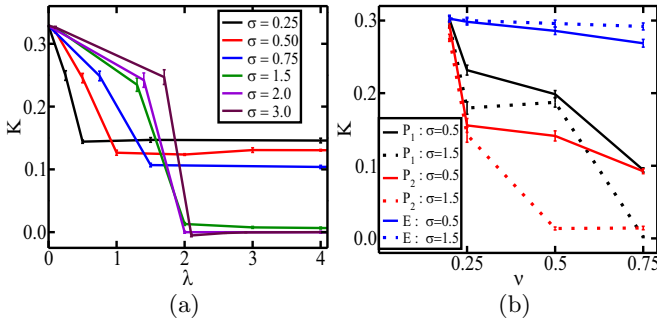
FIG. 8. (a) The prefactor K of the logarithmic term as a function of λ for fermions at half filling and for increasing values of σ. (b) K as a function of (no-special) filling fraction ν in the mixed phases P_1, P_2 and extended/delocalized (E) phase for $\sigma = 0.5$ and 1.5. For all plots, $N = 1024$ for α_g.

fermionic ground state at half filling. In the delocalized phase of a clean system for $\sigma > 0$, $K \approx 0.33$. When λ is turned on, the Fermi level at half filling in the P_2 phase becomes multifractal or localized for $\sigma < 1$ and $\sigma > 1$, respectively. In the P_1 phase, although being a mixed phase, the Fermi level and all other states below it remain delocalized at half filling with the values of K lying around 0.25. This shows that the nature of the delocalized states changes with λ. In the P_2 phase the values of K for the multifractal Fermi level (for $\sigma < 1$) decrease with σ showing the change in multifractality of the Fermi level with σ. $K \approx 0$ for $\sigma > 1$ as the Fermi level gets localized at half filling. In the $\sigma = \infty$ limit (AAH model [60,61]) $K \approx 0.33$, 0.26, and 0, respectively, in the delocalized phase, at the critical point and in the localized phase. In Fig. 8(b), we show K as a function of the nonspecial values of filling fraction ν. The plots show that in the extended/delocalized (E) phase K depends very little on ν whereas in the mixed phases (P_1, P_2) K may depend significantly on ν as shown in the figure for $\sigma = 0.5$ and 1.5.

VI. CONCLUSIONS

We uncover an intricate pattern of the localization structure of the AAH potential in the presence of long-range hoppings when the quasiperiodicity parameter is a member of the metallic mean family. In addition to the fully delocalized and localized phases, we obtain a coexistence of multifractal (localized) eigenstates with delocalized eigenstates for $\sigma < 1$ ($\sigma > 1$). The fraction of delocalized eigenstates in these phases can be obtained from a general sequence which is a manifestation of a mathematical property of the metallic mean family. The entanglement entropy of a noninteracting fermionic ground state respects the area law if the Fermi level belongs in the localized regime while logarithmically violating it if the Fermi level belongs in the delocalized or multifractal regimes, although the magnitude in the multifractal regime is significantly lower than in the delocalized one. A study of the prefactor of the logarithmically violationg term in the subsystem size scaling of entanglement entropy shows interesting behavior in different phases. The entanglement entropy surprisingly follows the area-law for certain special filling fractions even in the delocalized regime. These special filling fractions are related to the metallic means. In

this paper, we make an attempt to show how the inherent mathematical structure in the metallic means manifests itself in the single-particle and many-particle properties of a class of quasiperiodic models. Studies of this kind are very rare in the literature [62,63]. Hopefully, our work will help motivate further research in this direction.

In this Appendix, we discuss the results involving the IPR, fractal dimension, and entanglement entropy of the AAH model with nearest-neighbor hopping ($\sigma \to \infty$ limit of the LRH model) and quasiperiodic potential.

APPENDIX: IPR, FRACTAL DIMENSION, AND ENTANGLEMENT ENTROPY IN THE AAH MODEL

The AAH model has a self-dual point at $\lambda = 2$, where the Hamiltonian in position space maps to itself in momentum space. As a consequence, all the single-particle eigenstates are delocalized for $\lambda < 2$ and localized for $\lambda > 2$ [6,64]. But earlier studies [46,65] of the same model based on the golden mean as the quasiperiodicity parameter have shown the existence of energy-dependent localization properties. Here we extend the study to the case of metallic means. We discuss the results for various quantities ahead.

1. IPR

IPR of all single particle eigenstates for $\lambda = 1$ (delocalized phase) is shown in Fig. 9(a) for a non-Fibonacci $N = 1024$ and different values of α. There exist eigenstates with high IPR for fractional index $n/N = \alpha_g, \alpha_g^2, \alpha_g^3$ (≈ 0.618, 0.382, 0.236), etc. for the golden mean. Similarly, high-IPR eigenstates are also found for the cases of silver mean (α_s) and bronze mean (α_b) at $n/N = \alpha_s + \alpha_s^2, \alpha_s, \alpha_s^2 + \alpha_s^3, \alpha_s^2, \ldots$ ($\approx 0.58, 0.41, 0.24, 0.17, \ldots$), etc. and $n/N = 2\alpha_b + \alpha_b^2, \alpha_b + \alpha_b^2, \alpha_b, \ldots$ ($\approx 0.69, 0.39, 0.3, \ldots$), respectively. The single-particle energy spectra of these systems show large gaps at the positions where the high-IPR states exist [46] as shown in Fig. 9(c). In this figure, the level-spacing $\Delta_n = E_{n+1} - E_n$ with E_n being the energy of the nth eigenstate. Total number of level spacings $M = N - 1$.

These high-IPR eigenstates seem to vanish if N is chosen to be a Fibonacci number as shown in Fig. 9(b) for $\lambda = 1$ and $N = 610, 360$, and 408 for α_g, α_s, and α_b, respectively. However, we remark that the large gaps still continue to persist in the energy spectra as also shown in Fig. 9(d). The high-IPR eigenstates show an anomalous system-size dependence. As an example, we show the scaling of IPR of the special eigenstates with N in Fig. 10 for $\lambda = 1.0$ and α_g. Here N is restricted, respectively, to be non-Fibonacci and Fibonacci in Figs. 10(a) and 10(b). For non-Fibonacci N, the scaling behavior is severely anomalous and deviates from $1/N$. For Fibonacci N, the scaling behavior is less anomalous and close
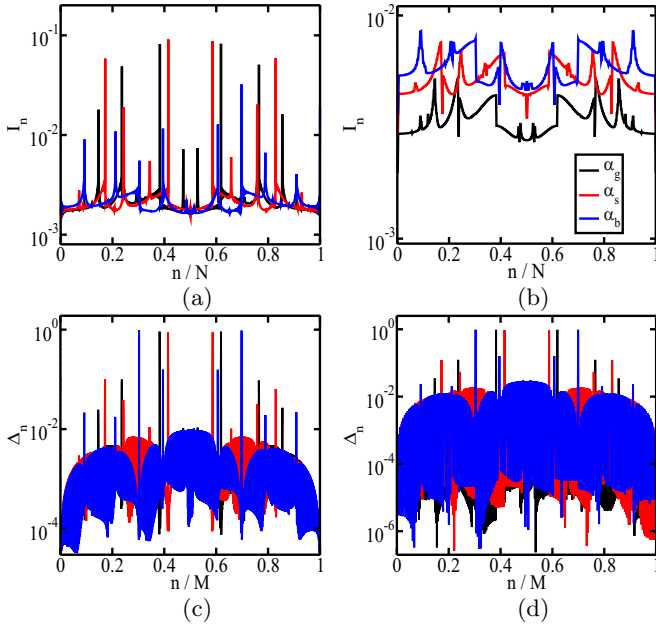
(a)

(b)

FIG. 9. (a) IPR of the single particle eigenstates I_n for different values of α and fixed $N = 1024$. (b) Similar plots for $N = 610$, 408, and 360 for α_g, α_s, and α_b, respectively. For these plots, n/N in the x axis stands for the fractional index of eigenstates. (c) Consecutive level-spacings $\Delta_n = E_{n+1} - E_n$ for different values of α and fixed $N = 1024$. (b) Δ_n's for $N = 610$, 408, and 360 for α_g, α_s, and α_b, respectively. n/M in the x axis stands for the fractional index of level spacings, where total number of spacings $M = N - 1$. For all plots, $\lambda = 1$ in the AAH model. The legend shown in (b) applies also to (a), (c), and (d).

to $1/N$ (although not exactly $1/N$), which is represented by the dashed line for nonspecial delocalized eigenstates.

2. Fractal dimension

The fractal dimension D_2 is calculated for each single particle eigenstate for $\lambda = 1$ and different parameters α_g, α_s, and α_b in a system of non-Fibonacci number of
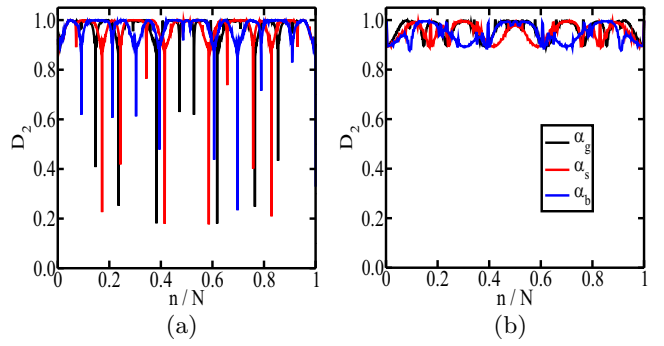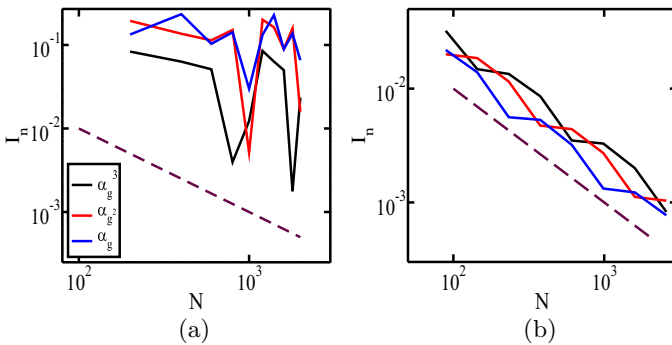

(a)

(b)

FIG. 10. (a) IPR of the special eigenstates with fractional index $n/N = \alpha_g^3, \alpha_g^2, \alpha_g$ as a function of system size N, which is a non-Fibonacci number. (b) Similar plots for N, which is a Fibonacci number corresponding to α_g. For all plots, $\lambda = 1$. The dashed line represents $1/N$ dependence of IPR of the nonspecial delocalized eigenstates.

(a)

(b)

FIG. 11. (a) Fractal dimension D_2 of the single-particle eigenstates for different values of α and fixed $N = 1000$. (b) Similar plots for $N = 610$, 408, and 360 for α_g, α_s, and α_b, respectively. For all plots, $\lambda = 1$ in the AAH model. n/N in the x axis stands for fractional index. Here $\delta = 1/N_l = 0.01$.

sites $N = 1000$ as shown in Fig. 11(a). In the delocalized phase, $D_2 \approx 1$ for the majority of the eigenstates. The large deviations from $D_2 \approx 1$ are observed at the fractional eigenstate index $n/N \approx \alpha_g, \alpha_g^2, \alpha_g^3$, etc. for α_g. Similar deviations can be seen at $n/N \approx \alpha_s + \alpha_s^2, \alpha_s, \alpha_s^2 + \alpha_s^3, \alpha_s^2$, etc. for α_s, and $n/N \approx 2\alpha_b + \alpha_b^2, \alpha_b + \alpha_b^2, \alpha_b$, etc. for α_b. For these special eigenstates, $0 < D_2 < 1$ which implies the presence of nondelocalized states. Figure 11(b) indicates that the large fluctuations of D_2 seem to vanish and D_2 is close to 1 for all the eigenstates when a Fibonacci number is chosen for N. This can be understood from Fig. 10(b).

In Fig. 12, we show the fractal dimension D_f as a function of f for the eigenstates with fractional index $n/N = \alpha_g^3, \alpha_g^2, \alpha_g$ for $\lambda = 1$ and golden mean α_g. In this figure, the solid lines represent the plots for Fibonacci $N = 610$ whereas the dashed lines represent the plots for non-Fibonacci $N = 1000$. We observe that the solid lines change very little with f and are close to 1. Here D_f deviates a little from 1 because these eigenstates are not perfectly delocalized as depicted in Fig. 10(b). On the other hand, the dashed lines show a small variation with f and their typical value is just a fraction of one. This indicates that for non-Fibonacci N, the special eigenstates with high IPR
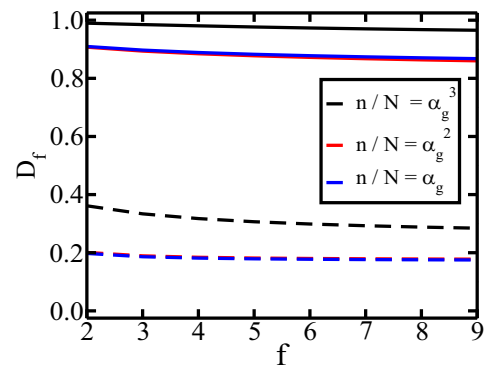

FIG. 12. Fractal dimension D_f as a function of f for the single particle eigenstates with fractional index $n/N = \alpha_g^3, \alpha_g^2, \alpha_g$. The solid lines represent plots for Fibonacci $N = 610$ whereas the dashed lines represent plots for non-Fibonacci $N = 1000$. For all plots, $\lambda = 1$, $\alpha = \alpha_g$ and $\delta = 1/N_l = 0.01$.
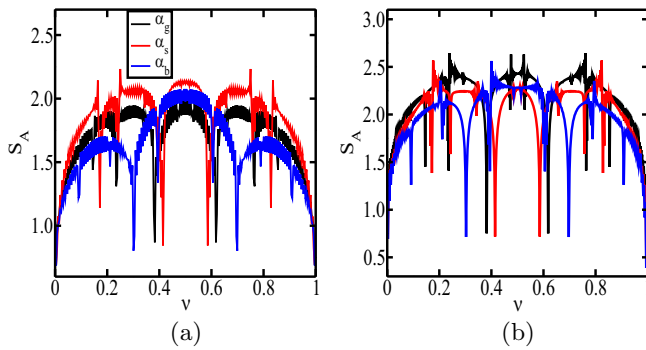
FIG. 13. (a) Entanglement entropy S_A of the ground state as a function of fermionic filling ν for different values of α and fixed $N = 256$. (b) Similar plots for $N = 610, 408$, and 360 for α_g, α_s, and α_b, respectively. For all plots, $\lambda = 1$ in the AAH model and size of subsystem A is $L = N/2$.

are weakly multifractal whereas for Fibonacci N, the special eigenstates behave more like the (imperfect) delocalized states like all other nonspecial states. This is true even for silver mean α_s and bronze mean α_b (not shown here).

3. Entanglement entropy

The ground-state entanglement entropy S_A of half the system (subsystem $L = N/2$) as a function of filling fraction ν for

$\lambda = 1$ is shown in Fig. 13(a) for a non-Fibonacci $N = 256$ and different values of α. Here $\nu = N_p/N$ where N_p and N are the number of particles and number of sites respectively. Similar to high IPR in Fig. 9(a), significantly low S_A is found at $\nu \approx \alpha_g, \alpha_g^2, \alpha_g^3$, etc. for α_g; $\nu \approx \alpha_s + \alpha_s^2, \alpha_s, \alpha_s^2 + \alpha_s^3, \alpha_s^2$ etc. for α_s; $\nu \approx \alpha_b + \alpha_b^2, \alpha_b + \alpha_b^2, \alpha_b$, etc. for α_b. But in contrast to Fig. 9(b) of IPR, the low S_A regions seem to persist as shown in Fig. 13(b) even for Fibonacci $N = 610, 408, 360$ for $\alpha_g, \alpha_s, \alpha_b$, respectively. The persisting imperfection of the special eigenstates (shown in Fig. 10) may be a reason behind this. The imperfection is captured at a magnified level by the many-particle entanglement entropy as compared to single particle IPR for a Fibonacci N. In the delocalized phase, $S_A \propto \ln L$ [46] for all values of ν except for the special values of ν where S_A abides by the area law with significantly smaller magnitudes. The signature of criticality in the model is absent for special ν. These properties of the special ν have been shown earlier in Ref. [46] for α_g and hold good for α_s and α_b also. However, the nonspecial half-filled ($\nu = 0.5$) ground state shows $S_A \propto \ln L$ both in the delocalized phase and at the critical point (almost $\ln L$) [60,61] whereas $S_A \propto L^0$ in the localized phase with the prefactor K of the logarithmic term being approximately $0.33, 0.26$, and 0, respectively. The logarithmic scaling at the critical point shows that the multifractal states are extended in nature but nonergodic as the prefactor differs from the ergodic delocalized ones.

[1] A. Goldman and R. Kelton, Rev. Mod. Phys. **65**, 213 (1993).

[2] M. Kohmoto, B. Sutherland, and C. Tang, Phys. Rev. B **35**, 1020 (1987).

[3] E. L. Albuquerque and M. G. Cottam, Phys. Rep. **376**, 225 (2003).

[4] E. Maciá, Rep. Prog. Phys. **69**, 397 (2005).

[5] P. W. Anderson, Phys. Rev. **109**, 1492 (1958).

[6] S. Aubry and G. André, Ann. Isr. Phys. Soc. **3**, 18 (1980).

[7] P. G. Harper, Proc. Phys. Soc. A **68**, 874 (1955).

[8] S. D. Sarma, S. He, and X. Xie, Phys. Rev. B **41**, 5544 (1990).

[9] S. Ganeshan, J. Pixley, and S. D. Sarma, Phys. Rev. Lett. **114**, 146601 (2015).

[10] Y. Lahini, R. Pugatch, F. Pozzi, M. Sorel, R. Morandotti, N. Davidson, and Y. Silberberg, Phys. Rev. Lett. **103**, 013901 (2009).

[11] E. Lucioni, B. Deissler, L. Tanzi, G. Roati, M. Zaccanti, M. Modugno, M. Larcher, F. Dalfovo, M. Inguscio, and G. Modugno, Phys. Rev. Lett. **106**, 230403 (2011).

[12] J. Lye, L. Fallani, M. Modugno, D. Wiersma, C. Fort, and M. Inguscio, Phys. Rev. Lett. **95**, 070401 (2005).

[13] M. Schreiber, S. S. Hodgman, P. Bordia, H. P. Lüschen, M. H. Fischer, R. Vosk, E. Altman, U. Schneider, and I. Bloch, Science **349**, 842 (2015).

[14] V. Oganesyan and D. A. Huse, Phys. Rev. B **75**, 155111 (2007).

[15] F. Alet and N. Laflorencie, C. R. Phys. **19**, 498 (2018).

[16] D. A. Abanin, E. Altman, I. Bloch, and M. Serbyn, Rev. Mod. Phys. **91**, 021001 (2019).

[17] S. Iyer, V. Oganesyan, G. Refael, and D. A. Huse, Phys. Rev. B **87**, 134202 (2013).

[18] R. Modak and S. Mukerjee, Phys. Rev. Lett. **115**, 230401 (2015).

[19] M. Žnidarič and M. Ljubotina, Proc. Natl. Acad. Sci. USA **115**, 4595 (2018).

[20] S. Xu, X. Li, Y.-T. Hsu, B. Swingle, and S. D. Sarma, Phys. Rev. Res. **1**, 032039(R) (2019).

[21] N. Nessi and A. Iucci, Phys. Rev. A **84**, 063614 (2011).

[22] N. Roy and S. Sinha, J. Stat. Mech. (2018) 053106.

[23] V. Michal, B. Altshuler, and G. Shlyapnikov, Phys. Rev. Lett. **113**, 045304 (2014).

[24] K. Kim, M.-S. Chang, S. Korenblit, R. Islam, E. E. Edwards, J. K. Freericks, G.-D. Lin, L.-M. Duan, and C. Monroe, Nature **465**, 590 (2010).

[25] P. Richerme, Z.-X. Gong, A. Lee, C. Senko, J. Smith, M. Foss-Feig, S. Michalakis, A. V. Gorshkov, and C. Monroe, Nature **511**, 198 (2014).

[26] J. W. Britton, B. C. Sawyer, A. C. Keith, C. C. J. Wang, J. K. Freericks, H. Uys, M. J. Biercuk, and J. J. Bollinger, Nature **484**, 489 (2012).

[27] R. Islam, C. Senko, W. C. Campbell, S. Korenblit, J. Smith, A. Lee, E. E. Edwards, C.-C. J. Wang, J. K. Freericks, and C. Monroe, Science **340**, 583 (2013).

[28] R. Löw, H. Weimer, U. Krohn, R. Heidemann, V. Bendkowsky, B. Butscher, H. P. Büchler, and T. Pfau, Phys. Rev. A **80**, 033422 (2009).

[29] H. Weimer, R. Löw, T. Pfau, and H. P. Büchler, Phys. Rev. Lett. **101**, 250601 (2008).

[30] H. Labuhn, D. Barredo, S. Ravets, S. de Léséleuc, T. Macrì, T. Lahaye, and A. Browaeys, Nature **534**, 667 (2016).

[31] P. Schauß, J. Zeiher, T. Fukuhara, S. Hild, M. Cheneau, T. Macrì, T. Pohl, I. Bloch, and C. Gross, Science **347**, 1455 (2015).

[32] S. Baier, D. Petter, J. Becher, A. Patscheider, G. Natale, L. Chomaz, M. Mark, and F. Ferlaino, Phys. Rev. Lett. **121**, 093602 (2018).

[33] A. V. Gorshkov, S. R. Manmana, G. Chen, E. Demler, M. D. Lukin, and A. M. Rey, Phys. Rev. A **84**, 033619 (2011).

[34] S. R. Manmana, E. M. Stoudenmire, K. R. A. Hazzard, A. M. Rey, and A. V. Gorshkov, Phys. Rev. B **87**, 081106(R) (2013).

[35] B. Yan, S. A. Moses, B. Gadway, J. P. Covey, K. R. A. Hazzard, A. M. Rey, D. S. Jin, and J. Ye, Nature **501**, 521 (2013).

[36] R. P. A. Lima, H. R. da Cruz, J. C. Cressoni, and M. L. Lyra, Phys. Rev. B **69**, 165117 (2004).

[37] A. D. Mirlin, Y. V. Fyodorov, F.-M. Dittes, J. Quezada, and T. H. Seligman, Phys. Rev. E **54**, 3221 (1996).

[38] G. Celardo, R. Kaiser, and F. Borgonovi, Phys. Rev. B **94**, 144206 (2016).

[39] X. Deng, V. E. Kravtsov, G. V. Shlyapnikov, and L. Santos, Phys. Rev. Lett. **120**, 110602 (2018).

[40] X. Deng, S. Ray, S. Sinha, G. Shlyapnikov, and L. Santos, Phys. Rev. Lett. **123**, 025301 (2019).

[41] S. Gopalakrishnan, Phys. Rev. B **96**, 054202 (2017).

[42] M. Saha, S. K. Maiti, and A. Purkayastha, Phys. Rev. B **100**, 174201 (2019).

[43] R. Modak and T. Nag, Phys. Rev. Res. **2**, 012074(R) (2020).

[44] J. Eisert, M. Cramer, and M. B. Plenio, Rev. Mod. Phys. **82**, 277 (2010).

[45] N. Laflorencie, Phys. Rep. **646**, 1 (2016).

[46] N. Roy and A. Sharma, Phys. Rev. B **100**, 195143 (2019).

[47] M. Modugno, New J. Phys. **11**, 033023 (2009).

[48] H. Cohn, Am. Math. Mon. **113**, 57 (2006).

[49] Y. Bugeaud, Math. Ann. **341**, 677 (2008).

[50] J. d. J. H. Serda, arXiv:1506.00144.

[51] S. Falcon, Appl. Math. **5**, 2226 (2014).

[52] A. Chhabra and R. V. Jensen, Phys. Rev. Lett. **62**, 1327 (1989).

[53] M. Janssen, Int. J. Mod. Phys. B **8**, 943 (1994).

[54] B. Huckestein, Rev. Mod. Phys. **67**, 357 (1995).

[55] E. Cuevas, Phys. Rev. B **68**, 184206 (2003).

[56] I. Peschel, J. Phys. A: Math. Gen. **36**, L205 (2003).

[57] I. Peschel and V. Eisler, J. Phys. A: Math. Theor. **42**, 504003 (2009).

[58] I. Peschel, Braz. J. Phys. **42**, 267 (2012).

[59] B. Swingle, Phys. Rev. Lett. **105**, 050502 (2010).

[60] N. Roy and A. Sharma, Phys. Rev. B **97**, 125116 (2018).

[61] G. Roósz, Z. Zimborás, and R. Juhász, Phys. Rev. B **102**, 064204 (2020).

[62] S. Thiem, M. Schreiber, and U. Grimm, Phys. Rev. B **80**, 214203 (2009).

[63] S. Thiem and M. Schreiber, Eur. Phys. J. B **83**, 415 (2011).

[64] S. Y. Jitomirskaya, Ann. Math. **150**, 1159 (1999).

[65] S. E. Skipetrov and A. Sinha, Phys. Rev. B **97**, 104202 (2018).